

Multi-Scale Modeling and Oxygen Impact on Tumor Temporal Evolution

Citation for published version (APA):

Apeke, S., Gaubert, L., Boussion, N., Lambin, P., Visvikis, D., Rodin, V., & Redou, P. (2018). Multi-Scale Modeling and Oxygen Impact on Tumor Temporal Evolution: Application on Rectal Cancer During Radiotherapy. *Ieee Transactions on Medical Imaging*, 37(4), 871-880. <https://doi.org/10.1109/TMI.2017.2771379>

Document status and date:

Published: 01/04/2018

DOI:

[10.1109/TMI.2017.2771379](https://doi.org/10.1109/TMI.2017.2771379)

Document Version:

Publisher's PDF, also known as Version of record

Document license:

Taverne

Please check the document version of this publication:

- A submitted manuscript is the version of the article upon submission and before peer-review. There can be important differences between the submitted version and the official published version of record. People interested in the research are advised to contact the author for the final version of the publication, or visit the DOI to the publisher's website.
- The final author version and the galley proof are versions of the publication after peer review.
- The final published version features the final layout of the paper including the volume, issue and page numbers.

[Link to publication](#)

General rights

Copyright and moral rights for the publications made accessible in the public portal are retained by the authors and/or other copyright owners and it is a condition of accessing publications that users recognise and abide by the legal requirements associated with these rights.

- Users may download and print one copy of any publication from the public portal for the purpose of private study or research.
- You may not further distribute the material or use it for any profit-making activity or commercial gain
- You may freely distribute the URL identifying the publication in the public portal.

If the publication is distributed under the terms of Article 25fa of the Dutch Copyright Act, indicated by the "Taverne" license above, please follow below link for the End User Agreement:

www.umlib.nl/taverne-license

Take down policy

If you believe that this document breaches copyright please contact us at:

repository@maastrichtuniversity.nl

providing details and we will investigate your claim.

Multi-Scale Modeling and Oxygen Impact on Tumor Temporal Evolution: Application on Rectal Cancer During Radiotherapy

Séna Apeke¹, Laurent Gaubert, Nicolas Bousson, Philippe Lambin, Dimitris Visvikis, Vincent Rodin, and Pascal Redou

Abstract—We present a multi-scale approach of tumor modeling in order to predict its evolution during radiotherapy. Within this context we focus on three different scales of tumor modeling: microscopic (individual cells in a voxel), mesoscopic (population of cells in a voxel) and macroscopic (whole tumor), with transition interfaces between these three scales. At the cellular level, the description is based on phase transfer probabilities in the cellular cycle. At the mesoscopic scale we represent populations of cells according to different stages in a cell cycle. Finally, at the macroscopic scale, the tumor description is based on the use of FDG PET image voxels. These three scales exist naturally: biological data are collected at the macroscopic scale, but the pathological behavior of the tumor is based on an abnormal cell-cycle at the microscopic scale. On the other hand, the introduction of a mesoscopic scale is essential in order to reduce the gap between the two extreme, in terms of resolution, description levels. It also reduces the computational burden of simulating a large number of individual cells. As an application of the proposed multi-scale model, we simulate the effect of oxygen on tumor evolution during radiotherapy. Two consecutive FDG PET images of 17 rectal cancer patients undergoing radiotherapy are used to simulate the tumor evolution during treatment. The simulated results are compared with those obtained on a third FDG PET image acquired two weeks after the beginning of the treatment.

Index Terms—Model, tumor, treatment response, discrete, stochastic, FDG PET image, microscopic, mesoscopic, macroscopic, simulation.

I. INTRODUCTION

CANCER is responsible for more than 8 million deaths worldwide each year (WHO fact sheet, updated January 2015). It is proved that the association of early diagnosis and prediction has a significant impact on overall survival rates [1]. Consequently the development of predictive and prognostic models for cancer treatment represents a field of increasing interest. Within this context the incorporation of tumor growth modelling, including interactions with response to treatment, is an essential element of prediction and prognosis models. A plethora of such tumor growth models has already been proposed and can be classified according to their theoretical framework; namely deterministic models, stochastic models [2]–[6] or agent-based models [7]. A model is deterministic if one considers that the system which is modelled is deterministic, *i.e.* a system in which no randomness is involved in the prediction of future states of the system. A deterministic model will thus always produce the same output from a given initial state. If one considers that the evolution of the system is based on random phenomena, the associated model which predicts its evolution is stochastic. Finally, the agent-based modelling or simulation is segmented in various entities which interact: each agent represents an individual or a group of individuals.

The currently proposed continuous stochastic models for tumor growth [8], [9] are not intended to describe the interactions between the various scales which can intervene, and which represent one of the main issues for describing biological and radio-biological phenomena. On the other hand, although modelling at the macroscopic scale aims at predicting the overall tumor behaviour, system observations are made on cell groups for discrete models, or on cell densities for continuous models [10].

As such, one of the major difficulties in tumor growth modelling is the relationship between the microscopic and macroscopic model states. One may consider starting from a microscopic scale with the simulation of a large number of cells and their evolution in order to reach the observations at a macroscopic level. However, the number of cells needed

Manuscript received August 25, 2017; revised October 31, 2017; accepted November 2, 2017. Date of publication November 8, 2017; date of current version April 2, 2018. This work was supported in part by Bretagne Region and in part by LaTIM. (Corresponding author: Séna Apeke.)

S. Apeke is with Inserm, UMR 1101, Brest, F-29200 France, and also with the IHSEV, CID, Lab-STICC, UMR CNRS, Computer Science Department, Université de Bretagne Occidentale, 29238 Brest, France (e-mail: kodjo-sena.apeke@univ-brest.fr).

L. Gaubert and P. Redou are with Inserm, UMR 1101, F-29200 Brest, France, and also with CERV, European Center for Virtual Reality, École nationale d'ingénieurs de Brest, 29280 Brest, France.

N. Bousson is with Inserm, UMR 1101, 29200 Brest, France, and also with CHRU BREST, 29200 Brest, France.

P. Lambin is with Maastrro (Maastricht Radiation Oncology), GROW School for Oncology and Development Biology, Maastricht University Medical Centre, Maastricht 6211, The Netherlands.

D. Visvikis, and are with Inserm, UMR 1101, Brest, 29200 France, and also with CHRU BREST, 29200 Brest, France.

V. Rodin is with IHSEV, CID, Lab-STICC, UMR CNRS, Computer Science Department, Université de Bretagne Occidentale, 6285 Brest, France.

Color versions of one or more of the figures in this paper are available online at <http://ieeexplore.ieee.org>.

Digital Object Identifier 10.1109/TMI.2017.2771379

for such an approach leads to a computational burden which is too high to be of any clinical relevance. On the other hand, the consideration of a smaller number of cells clearly compromises the accuracy of the model at the macroscopic level. For continuous models an intermediate phase can be used, known as the kinetic or mesoscopic scale, which induces a probability distribution. A mesoscopic scale is closely associated with inputs from both macroscopic (global patient data) and microscopic (cellular) scales.

The first aim in this work is to provide a consistent and explicit multi-scale model, embedding interfaces between the different description levels. In addition, an analysis of algorithmic complexity points to the interest of a mesoscopic scale from a computational efficiency point of view. A second goal of this work is the application of the proposed model to tumor growth and response to radiotherapy outcome prediction, using the tumor oxygen pressure as an adjustment parameter. Many previous studies have focused on the prediction of the variation in the number of proliferating, hypoxic and necrotic cells according to oxygen pressure distribution, which in turn depends on many different parameters (for example the HIF-1alpha factor [11], the activation of a signal for cell apoptosis or quiescence [12]). Heterogeneity of oxygen pressure is also a factor which allows to distinguish various tumor cell classes [5], [11], [12]. In this work we have used a two step evaluation process for the proposed model within the specific context of radiotherapy treatment. Based on the first two FDG PET images of a patient under treatment, we estimate an oxygen pressure level using the proposed model. In this first step, the proposed interface between macroscopic and microscopic scales is assessed, with the use of the oxygen pressure as a parameter which influences the cellular transition probabilities within a cell cycle. Finally, the total number of simulated tumor cells is compared to the one obtained when using clinical FDG images acquired at day 15 of the radiotherapy treatment protocol.

II. MATERIALS AND METHODS

A. Model Description and Conception

In this section we present the three different scales used in the proposed modelling paradigm. The time variable is denoted by t , but for the sake of simplicity we will often omit this variable. For instance, a variable $x(t)$ that evolves along time will often be referred to as x .

1) *Macroscopic Scale E_1* : The data used in this study at the macroscopic scale are FDG PET images, routinely in use for diagnosis, staging, and response to therapy assessment [13]. At this scale, the model is constructed using the following components:

- *Parameters*: the number of voxels in an FDG PET image is $N_{vox} = N_x \times N_y \times N_z$, where N_x , N_y and N_z are the number of voxels in each direction;
- *Variables*: intensity in each voxel is denoted by i_{vox} .

2) *Microscopic Scale E_3* : As mentioned earlier, in order to handle tumor growth at this scale, the approach is based on the cellular division principle and managed cell by cell. Indeed, metabolism, nutrition and cellular death (natural

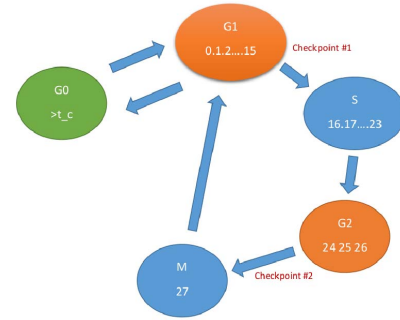


Fig. 1. Different phases of cell cycle annotated as they are used within the proposed model; t_c is the cell cycle time period (here $t_c = 28h$).

or not) are all phenomena that take place at the cellular scale and are strongly involved in cellular division. Cell division probability and cell survival probability after radiotherapy depend, amongst other parameters, on the oxygen pressure and are thus estimated at the microscopic scale. Since one of the main attributes of a cell is its state within the cell cycle, we briefly recall here the different states of a mammalian cell:

- Gap 0 or G_0 is the quiescent state of a cell, a resting phase when it has left the cycle and stopped dividing;
- In Gap 1 or G_1 phase, the cell grows in size;
- S is the synthesis phase where DNA replication occurs;
- G_2 is the phase between DNA synthesis and mitosis, the cell will continue to grow in this gap;
- Mitosis or M is the last phase of cell division. Cell growth stops at this stage and cellular energy is focused on the orderly division into two daughter cells.

Based on [14], we suppose here that the cellular cycle lasts 28 hours; on average, a cell spends 16 hours in G_1 phase, 8 hours in S phase, 3 hours in G_2 phase and finally one hour in the mitosis phase (Figure 1). A cell which is in none of these stages is quiescent or dead. Regarding the transition processes, there are three specific steps: two random tests that control transitions from G_1 to S and from G_2 to M and a random test of survival after radiotherapy. The simulation time step was chosen as 1 hour long.

More precisely, let us consider a cell that has just arrived in phase G_1 . The first time the transition process is applied, it simply increases the time spent in the phase by 1, and so on until the cell has spent 15 hours in phase G_1 . At this time, the process randomly decides whether the cell stays in phase G_1 , having spent 16 hours there, or if it goes into S phase, with a “spent time” equal to 16. Transition from S to G_2 is automatic, but at the end of G_2 there is a similar random test. Tests at checkpoints (Figure 1) are modelled by the Bernoulli’s Law $B(p)$ and the probability p for both transitions (from G_1 to S and from G_2 to M) depends on the level of oxygen pressure. The transitions G_1/S and G_2/M are strongly influenced by the environment in which cells evolve and divide, in particular by hypoxia [15]. We thus model these transitions by Gompertz distribution [16] depending on the pO_2 level, as in [5].

$$\begin{cases} p = P(pO_2) \\ = C. \exp(-\exp([-B(pO_2 - pO_2^{infl})])) \end{cases} \quad (1)$$

where, C is the superior asymptote, B the growth rate, pO_2^{infl} represents the pO_2 value at curve inflexion point and pO_2 the oxygen partial pressure [5].

Regarding treatment response modelling, a cell in any phase of the cellular cycle can die or survive according to the delivered dose. A linear-quadratic model (LQM, see [17], [18]) was used to assess the survival probability of a given cell after irradiation, as in [19] or [20]:

$$P_{survival}(Dose) = \exp\left(-\alpha \cdot Dose \left(1 + Dose \frac{\beta}{\alpha}\right)\right) \quad (2)$$

where, α and β are coefficients of radio-sensitivity. These parameters have been considered constant throughout the treatment, given that there is currently no consistent radiobiological data demonstrating their potential temporal evolution during treatment [21]. Since proliferating cells are less resistant to radiotherapy compared to hypoxic cells, the LQM [20] model depends on the oxygen partial pressure available for one cell or for the cell population:

$$\begin{cases} z = \left(1 + \frac{\beta}{\alpha} \cdot Dose \cdot OMF(pO_2)\right) \\ q = P_{survival}(Dose, pO_2) \\ = \exp(-\alpha \cdot Dose \cdot OMF(pO_2) \cdot z) \end{cases} \quad (3)$$

In these formulas, q is the surviving cells fraction after irradiation and the Oxygen-dependent Modification Factor (OMF) [5], [6] is given by pO_2 :

$$OMF(pO_2) = \frac{m \cdot pO_2 + k}{m(pO_2 + k)} \quad (4)$$

where, m is the maximum ratio and k is the pO_2 at half of the increase from 1 to m [5].

At this scale and for each voxel, the model can be therefore summarized by the following components:

- Parameters are radio-sensitivity coefficients α and β [5], oxygen pressure pO_2 and the dose delivered at each fraction, $Dose$;
- Variables will be presented as lists $(x_i)_{i=1 \dots N_{cell}}$ for each voxel, with every cell represented by two attributes; namely the phase of cellular division is denoted by X ($X \in \{G_0, G_1, S, G_2, M\}$), and the time spent in this phase h ;
- Rules: the evolution of a cell is based on rules detailed above.

3) Mesoscopic Scale E_2 : As already mentioned the aim of this intermediate modelling scale is to allow an efficient compromise between accuracy and computational efficiency.

At the microscopic scale E_3 , the transition process is applied to every single cell, which induces numerous computational loops and random numbers generation. A simple alternative is to factorize the application of the transition processes. For example, all cells that have spent one hour in phase G_1 will evolve in the same way: the phase remains the same, and the time spent in this phase is incremented. Therefore, it is efficient to create a variable that stores the number of cells that have spent one hour in phase G_1 , and so on. Regarding the cells that may or may not pass a checkpoint, the transition process involves the generation of random numbers, one for each cell. Considering the variable that represents the number

of cells that will attempt to pass the checkpoint, we can observe that the number of cells that succeed in this test is a binomial random variable. Thus one may significantly increase the speed of the process by approximating this random variable by a Gaussian one, when appropriate.

More precisely for each cell, the transition tests from G_1 to S or from G_2 to M are modelled by a random variable X_i with Bernoulli distribution $B(p)$. Therefore, the number of cells which succeed the test at checkpoint #1 (see Figure 1) and will be at the following time step in the synthesis phase is a random variable Z which follows binomial distribution with parameters $N_{G_1}^{(15)}$ (number of cells at step 15 of G_1), and p :

$$Z = \sum_{i=1}^{N_{G_1}^{15}} X_i \leftrightarrow \mathcal{B}\left(N_{G_1}^{15}, p\right) \quad (5)$$

The number of cells in the different phase compartments is generally much larger than 50, so if we assume that the probability of success of the test is neither close to 0, nor to 1, we can approximate the binomial distribution Z by a normal distribution with parameters $pN_{G_1}^{15}$ and $\sqrt{p(1-p)N_{G_1}^{15}}$, *i.e.*

$$Z \leftrightarrow Y = \mathcal{N}\left(pN_{G_1}^{15}, \sqrt{p(1-p)N_{G_1}^{15}}\right) \quad (6)$$

A comparable approximation is defined at checkpoint #2. In a similar way, right after a radiation dose delivery, since a fraction of all cells will die, the cell number in each sub-population is given by a normal distribution (6):

$$\mathcal{N}\left(qN_X, \sqrt{q(1-q)N_X}\right) \quad (7)$$

where, q is given by (3) and $X \in \{G_0, G_1, S, G_2, M\}$.

Accordingly, we specify the model at this scale with the following components:

- Parameters α and β , oxygen pressure pO_2 and $Dose$ are the same as described above;
- Variables: N_X^h is the number of cells that have been in phase X for h hours ($X \in \{G_1, S, G_2, M\}$) and N_{G_0} the number of cells in quiescence phase;
- Rules: for simplicity, we use the following notations; N_X is the number of cells in phase X and $N_{X/Y}$ is the number of cells which go from phase X to phase Y . The following equations describe the evolution of the system state, *i.e.* the tumor evolution.

$$N_{G_1}^0(t+1) = 2N_M^{27}(t) \quad (8)$$

$$N_{G_1}^{j+1}(t+1) = N_{G_1}^j(t), \quad 0 \leq j \leq 13 \quad (9)$$

$$N_{G_1}^{15}(t+1) = N_{G_1}^{14}(t) + \underbrace{N_{G_1}^{15}(t) - N_{G_1/S}(t)}_{test=false} \quad (10)$$

$$N_S^{16}(t+1) = N_{G_1/S}(t) \quad (11)$$

$$N_S^{j+1}(t+1) = N_S^j(t), \quad 16 \leq j \leq 22 \quad (12)$$

$$N_{G_2}^{24}(t+1) = N_S^{23}(t) \quad (13)$$

$$N_{G_2}^{25}(t+1) = N_{G_2}^{24}(t) \quad (14)$$

$$N_{G_2}^{26}(t+1) = N_{G_2}^{25}(t) + \underbrace{N_{G_2}^{26}(t) - N_{G_2/M}(t)}_{test=false} \quad (15)$$

$$N_M^{27}(t+1) = N_{G_2/M}(t) \quad (16)$$

$$N_{G_0}(t+1) = N_{G_0}(t) - N_{G_0/G_1}(t) + N_{G_1/G_0}(t) \quad (17)$$

TABLE I
LIST OF PARAMETERS USED IN THIS WORK

Parameter	symbol	Value and reference
Maximum OMF value	m	3 [5]
pO_2 at OMF = (m+1)/2	k	3 mmHg [5]
Radio-sensitivity coefficient	α	0.044 Gy^{-1}
Radio-sensitivity coefficient	β	0.089 Gy^{-2}
Cell density per mm^3	μ	10^6 [20]
Cell division maximum probability	C	1
Cell growth rate	B	0.075 [22]
pO_2 value at curve inflexion point	pO_2^{infl}	26.8 [23]
Voxel volume	voxel_v	$5.31 \times 5.31 \times 3mm^3$

Equations (8) - (10) update the number of cells in every compartment of the phase G_1 every hour, $N_{G_1/S}(t)$ represents the number of cells which have been successful at the checkpoint test from compartment 15 of G_1 phase to the first compartment of synthesis phase S . Equations (11) - (16) update each hour the number of cells in every compartment of phases S , G_2 , M and G_0 . $N_{G_2/M}(t)$ represents the number of cells which have been successful at the checkpoint test from compartment 26 of G_2 phase to the first compartment of mitosis phase M . Regarding equation (17), the transition G_1/G_0 is based on the level of pO_2 . If pO_2 in G_1 is very low ($< 2 mmHg$), cells remain blocked in G_1 , in other words they are in quiescence, otherwise they continue the stages of the division.

B. Scale Interfaces

This section describes the interactions between the different scales and associated variables.

1) *From Macroscopic to Mesoscopic Scale $E_1 \rightarrow E_2$* : In a voxel, given i_{vox} , one computes the number N_{cell} of tumor cells (see equation (22) below). Subsequently, one must divide this number among all the variables of the mesoscopic scale: N_X^h , with $X \in \{G_1, S, G_2, M, G_0\}$ and $0 \leq h \leq 28$, as described in equations (8) to (16). Since the mesoscopic model is a Markov chain, we assume an initial stationary distribution λ (see appendix for details). Thus, let $\lambda = (\lambda_{G_1}^0, \lambda_{G_1}^1, \dots, \lambda_M^{27}, \lambda_{G_0}^{28}) \in \mathbb{R}^{29}$ be this stationary distribution of the N_{cell} cells in the various phases of the cellular cycle.

We assign the variables at the mesoscopic scale in the following way (where $\lfloor \cdot \rfloor$ is the floor function):

$$N_X^h = \lfloor N_{cell} \cdot \lambda_X^h \rfloor \quad (18)$$

where, $X \in \{G_1, S, G_2, M, G_0\}$, $0 \leq h \leq 28$. This may be written as:

$$N = \lfloor N_{cell} \cdot \lambda \rfloor \quad (19)$$

where, $N = (N_X^h)_{h,X}$

2) *From Mesoscopic to Macroscopic Scale $E_2 \rightarrow E_1$* : Given the mesoscopic variable N , denoting the distribution of the cells in the different phases of the cell cycle in a voxel, the macroscopic variable N_{cell} is the sum of all the components of N :

$$N_{cell} = \sum_{h,X} N_X^h \quad (20)$$

from which we deduce i_{vox} (equation (22)).

3) *From Mesoscopic to Microscopic Scale $E_2 \rightarrow E_3$* : Given the mesoscopic variables N_X^h , one must obviously attribute exactly N_X^h cells with the corresponding attributes: the phase is X and the time spent in this phase is h .

4) *From Microscopic to Mesoscopic Scales $E_3 \rightarrow E_2$* : Given the list of individual cells in an image voxel, a mesoscopic variable N_X^h is simply the number of cells which have been in phase X for h hours.

C. Mesoscopic vs Microscopic

A comparison between microscopic and mesoscopic scales is considered in this study, from a computational complexity point of view. The mesoscopic model algorithmic complexity is based on equations (8) to (17). This complexity is thus constant whatever the value of N_{cell} , whilst in the microscopic scale, the loop on the evolution of cells in the various phases of the cellular cycle is handled cell-by-cell, each cell executing various functions. These functions include checkpoint tests and cell division functions, for which time complexity varies linearly with N_{cell} . These functions being called N_{cell} times, this leads to an execution time of the algorithm which grows as $N_{cell} \cdot update(N_{cell})$, i.e. at the microscopic scale the algorithm has a running time that grows proportionally to $update(N_{cell}) \cdot N_{cell} \cdot update(N_{cell})$ is a function that updates N_{cell} at each iteration step. This function has the following shape:

$$update(N_{cell}) = \varsigma \cdot N_{cell} \quad (21)$$

where, $0 < \varsigma < 1$ during radiotherapy.

D. Application Using Clinical PET Images

FDG PET images and a fixed oxygen pressure distribution were the input data of the proposed model. The output was given by altered FDG images in which the total number of tumor cells was also computed. Three FDG PET images (Figure 2) were acquired for each of the 17 patients included in this study. The first image was acquired several days before the first treatment day (min 4 days, max 11 days). The second and third images were acquired one week and two weeks after the beginning of the treatment respectively. For each patient the prescribed radiotherapy dose was 45 Gy in total, delivered daily from Monday to Friday during 5 weeks (1.8 Gy per day) except weekends. FDG images were segmented using FLAB (a Bayesian-based functional image segmentation algorithm [24], [25]) in order to ensure the model and associated simulation are applied only on the tumor region of interest. This segmentation algorithm has been extensively used in PET imaging for the segmentation of tumor functional volumes, showing improved accuracy, reproducibility and robustness relative to thresholding approaches [24].

We assumed that the number of tumor cells is proportional to the glucose consumption as previously considered by [5] and [19]. In order to calculate the initial number of active cells in each image voxel, the voxel with the maximal intensity was supposed to contain only active and capillary cells. Fractions of capillary cells and active tumor cells were

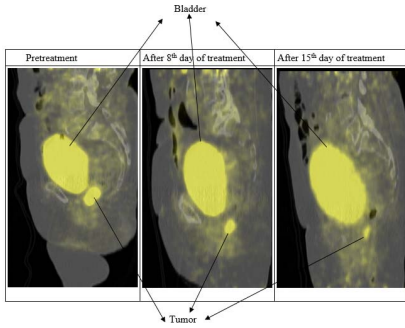


Fig. 2. Example of FDG PET images (rectal cancer).

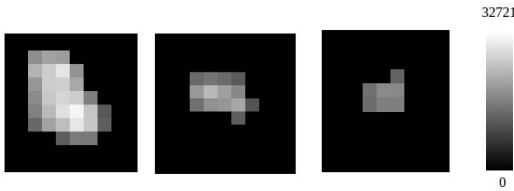


Fig. 3. Segmentation of the Figure 2 to get the tumor regions of interest (the tumor).

$\mu_c = 3.6\%$ and $\mu_t = 96.4\%$ respectively [20]. Denoting by i_{max} the maximal intensity among all voxel intensity values, the number of active cells (N_{cell}) in each voxel is given by:

$$N_{cell} = \frac{i_{vox}}{i_{max}} \cdot voxel_v \cdot \mu_t \cdot 10^6 \quad (22)$$

Therefore, a modified PET image can be obtained at every moment during the simulation process by simply taking into account the updated value of N_{cell} .

E. Model Evaluation

The first two FDG PET images were used to infer the oxygen pressure distribution map, and subsequently used to simulate the tumor evolution during the treatment. The simulated results were compared to those obtained on the third FDG PET image acquired two weeks after the beginning of the radiotherapy treatment.

More precisely, this oxygen pressure distribution was estimated by comparing the modelled and clinical FDG images after 8 days of treatment. To this end, the predicted and clinical total number of tumor cells are denoted respectively by N_p and N_c , and given by:

$$N_L = \sum_{k=1}^{N_{box}} \sum_{X \in \{G_0, G_1, S, G_2, M\}} N_{X,L}^k \quad (23)$$

where, $L \in \{p, c\}$.

Thus, the correlation between these two numbers is defined by:

$$correlation(\%) = \left(1 - \frac{|N_p - N_c|}{N_c}\right) \cdot 100 \quad (24)$$

To estimate the oxygen partial pressure distribution, four classes of voxels were considered, according to their intensity. For each voxel, one calculates the number of cells it contains. The same value of partial oxygen pressure was assigned to all voxels whose number of tumor cells belongs to the same interval. This value is considered as the average oxygen partial pressure in this interval. Concretely, for a given patient image, we calculate the intensities: minimum (i_{min}), first quartile (i_{Q_1}), median (i_{med}), third quartile (i_{Q_3}) and maximum (i_{max}). Then, in each voxel, pO_2 is defined as follows:

$$pO_2 = \begin{cases} u_1, & \text{if } i_{min} \leq i_{vox} \leq i_{Q_1} \\ u_2, & \text{if } i_{Q_1} < i_{vox} \leq i_{med} \\ u_3, & \text{if } i_{med} < i_{vox} \leq i_{Q_3} \\ u_4, & \text{if } i_{Q_3} < i_{vox} \leq i_{max} \end{cases} \quad (25)$$

where, u_i denotes the value of the partial pressure of oxygen for all i ($i = 1, 2, 3, 4$). The optimal quadruplet (u_1, u_2, u_3, u_4) was determined by using the correlation between the simulated and acquired images at the 8th day after the first irradiation. Before calculating the optimal values of u_i , we studied a sensitivity analysis of these values on the output of the model, using Sobol sensitivity indices [26], [27]. The idea of this method is to quantify the importance of an input parameter on the variance of $Y = f(u)$, considered as a random variable. Y is a scalar output of the model, namely:

$$Y = f(u) = \left(1 - \frac{N_p(u)}{N_c}\right)^2, u = (u_1, u_2, u_3, u_4) \quad (26)$$

Denote by $U_i, i = 1, 2, 3, 4$, the independent random variables with the same law (uniform law in this study), whose realizations are the inputs u_i . To evaluate the importance of an input parameter on the variance of Y , Sobol studies the conditional variance of the output Y , for a given u_i : $V(Y|U_i = u_i)$. This raises the problem of the choice of u_i . To solve this problem, it considers the possible values of u_i , calculating the variance of the conditional expectation of Y given U_i : $V(E[Y|U_i])$. Thus, the first order Sobol's indice of the parameter u_i is given by:

$$S_i = \frac{V(E[Y|U_i])}{V(Y)} \quad (27)$$

These indices were calculated using a Monte Carlo method, for integral computation approximation. See article [26], [27] for the calculation of the total sensitivity indice of a parameter.

It should be noted that the data used in this study were acquired over a period of two-weeks; one week between the initial image (pretreatment) and the image at the 8th day after the start of treatment, followed by one extra week for the image acquired at the 15th day after the start of treatment. This two weeks, period being short (except for aggressive tumors), so that we assume the partial pressure distribution of pO_2 is constant over time.

The oxygen pressure distribution which led to the best correlation was used in the simulation until the end of the radiotherapy treatment session. Mesoscopic data for each

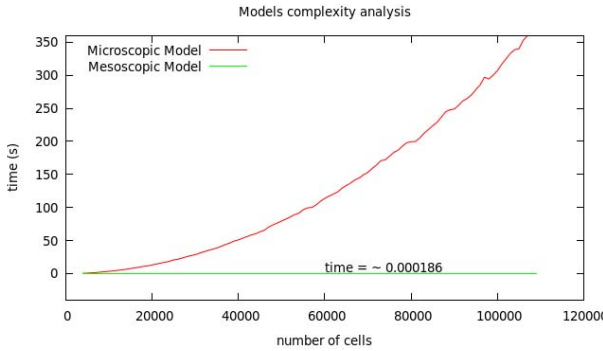


Fig. 4. Execution time for the microscopic and the mesoscopic models as a function of the number of tumor cells in a voxel.

simulation, *i.e.* the initial distribution of cells amongst phases of the cycle, were calculated by using the interactions between scales. The oxygen pressure distribution was then changed iteratively by using a gradient method, in order to determine the distribution which led to the best correlation between real and simulated total number of tumor cells after 8 days of daily radiotherapy.

III. RESULTS

A. Complexity Analysis

To compare the complexity and associated computational efficiency of the models at the microscopic [5] and mesoscopic scales, both models were executed using the same conditions and computer architectures.

According to equations (8) - (17) and the successive functions called in the simulation of these equations, the complexity of the mesoscopic model was in the affine form:

$$Complexity_{Meso} = a_1 \times N_{vox} + a_2 \quad (28)$$

Similarly, based on [5], the microscopic model complexity was in the form:

$$Complexity_{Micro} = N_{vox} \cdot (\zeta \cdot N_{cell}^2 + b_1 \cdot N_{cell} + b_2) \quad (29)$$

where, N_{vox} is the number of voxels in the ROI, a_1 , a_2 , b_1 , b_2 are positive constants.

To illustrate this result, a comparison of computation times was performed with respect to the number of tumor cells ranging from $6 \cdot 10^3$ to 0.1×10^6 inside a single voxel. As one can notice from Figure 4, the execution times for the mesoscopic model are independent from the simulated number of cells. For a single voxel, the computational time of the microscopic model has a parabolic growth, while that of the mesoscopic model remains constant with increasing number of cells.

B. Estimation of the Average Tumor Oxygen Partial Pressure

The results for the sensitivity analysis are presented in Table II. As shown in this table, u_3 and u_4 are very sensitive, *i.e.* a small variation of u_3 and u_4 leads to a non-negligible variation of the output of the model. This result is normal,

TABLE II
THE FIRST ORDER EFFECTS AND TOTAL EFFECTS FOR SENSITIVITY ANALYSIS OF THE VALUES u_j

Parameter #	1st Order effects	Total effects
u_1	0.0235294	0.0192255
u_2	0.0107583	0.00041467
u_3	0.378117	0.32160
u_4	0.469636	0.647769

TABLE III
OXYGEN PARTIAL PRESSURE DISTRIBUTION ESTIMATION USING THE MESOSCOPIC MODEL, RESULTS WERE OBTAINED BY COMPARING THE CLINICAL IMAGES AFTER THE 8th DAY OF TREATMENT OF 17 RECTAL CANCER PATIENTS WITH THE CORRESPONDING SIMULATED IMAGES (EQ 24)

Patient #	correlation day 8 (%)	u_1	u_2	u_3	u_4
1	99.86	7.902	4.445	2.502	2.50
2	99.89	8.922	11.478	13.059	3.99
3	96.25	2.0	1.00	1.5	2.00
4	99.00	5.942	10.552	11.036	5.99
5	95.42	10.982	10.97	8.966	5.99
6	99.55	1.799	2.499	1.80	0.70
7	99.22	3.18	9.65	8.483	6.00
8	99.26	4.1	9.77	3.975	7.99
9	98.86	4.055	2.01	8.001	5.69
10	98.80	8.941	10.82	4.099	9.00
11	99.24	7.82	11.33	11.97	6.00
12	99.10	1.39	1.799	1.40	0.499
13	99.98	3.00	5.022	1.30	2.00
14	99.51	3.82	10.175	5.54	7.99
15	99.96	4.103	10.42	11.593	3.99
16	92.01	1.199	2.10	1.599	0.80
17	95.67	10.944	10.756	9.571	3.50

since they correspond to the values of pO_2 in the voxels where there are more tumor cells, allowing to evaluate the smooth running of the model. The results of optimal values which characterize the optimal distribution of the pO_2 for all the patients, were presented in Table III.

C. Simulation of the Temporal Evolution of Tumor Cells Population

Using the optimal distribution of the oxygen partial pressure as the input of the model, we have evaluated the evolution of the total number of tumor cells. Figure 5 shows the temporal evolution of the total number of tumor cells. In Figure 5(a) one can notice the increase in the total number of tumor cells between time 0 and time 185 h which corresponds to the period before the first radiotherapy dose delivery. After this initial phase, the effect of radiotherapy becomes visible with daily decreases of tumor cells followed by a recovery corresponding to the period without treatment. Similar results for specific cells in each phase of the cellular cycle are showed in Figure 5(b). Figure 6 shows the tumor FDG PET images corresponding to patient 11; (a). clinical images: before, one week and two weeks after the start of radiation treatment, and (b). simulated after one and two weeks of treatment.

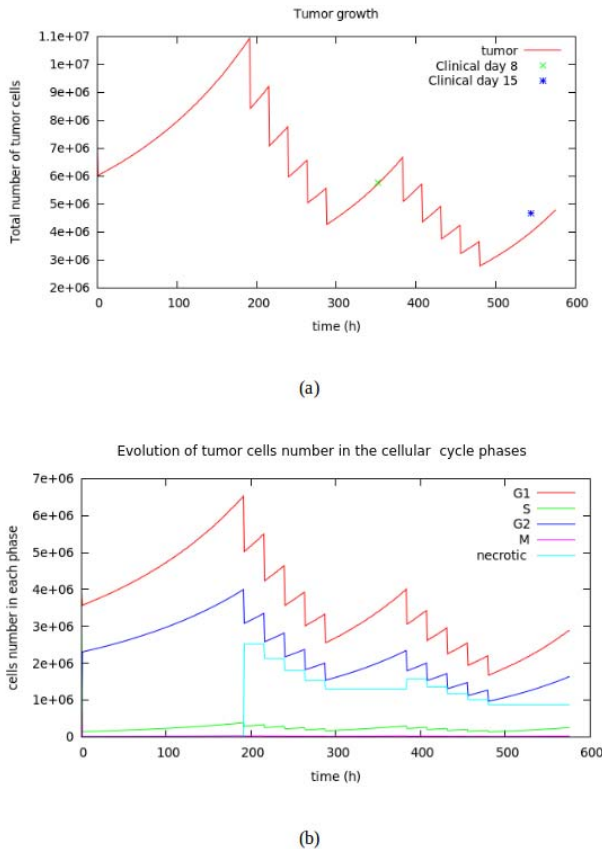


Fig. 5. The evolution of tumor cell number during the treatment according to the optimal pO_2 distribution for patient 11; (a). global and (b). in each phase of the cellular cycle.

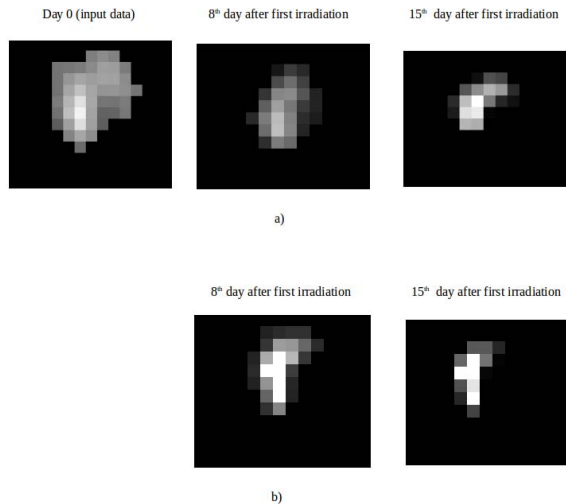


Fig. 6. (a) Clinical and (b) simulated images for patient 11.

A comparison between the acquired (Figure 6(a) Day 15) and predicted (Figure 6(b) Day 15) FDG images shows a similar behavior in terms of tumor size.

Correlations between the global number of tumor cells in predicted and clinical FDG PET images during radiotherapy treatment is shown in Table IV. As shown in this table, almost all correlations between the measured and predicted populations, at 8th day after the beginning of the treatment, are higher

TABLE IV

THIS TABLE SHOWS, ACCORDING TO THE OXYGEN DISTRIBUTION VALUES GIVEN IN TABLE III, THE CORRELATION BETWEEN THE GLOBAL NUMBER OF TUMOR CELLS IN PREDICTED AND CLINICAL FDG PET IMAGES AFTER 8 AND 15 DAYS OF TREATMENT (2nd AND 3rd COLUMN RESPECTIVELY)

Patient #	correlation at 8th day (%)	correlation at 15th day (%)
1	99.8636	69.2573
2	99.8914	92.3391
3	96.2490	84.7743
4	99.00	41.046
5	95.419	88.504
6	99.55	92.306
7	99.2231	54.5509
8	99.264	72.413
9	99.8053	53.4206
10	98.796	80.366
11	99.2434	85.4142
12	99.104	99.656
13	99.98	84.056
14	99.5125	70.4836
15	99.9618	70.2106
16	92.0599	81.7025
17	95.67	90.56

than 90%, while for the 15th day after the beginning of the treatment, the statistics are as follows: for 10/17 patients there is a high global correlation (considering both 8 and 15 days into the treatment) superior to 80%, for 4/17 patients an averages correlation of 60 – 80%, and for 3/17 patients a global correlation of <60%.

IV. DISCUSSION

In this study, FDG PET images acquired from 17 patients were used to evaluate a new model for the simulation of tumor growth and response to radiotherapy treatment. Two major objectives included a new interfacing approach between microscopic and macroscopic scales, as well as demonstrating the impact of oxygen pressure in such a modelling approach. The population scale modelling for simulation of tumor growth presented in this study demonstrates an interest compared to an individual microscopic scale model, in terms of computational efficiency without loss of accuracy. Indeed, the voxel size in PET images leads to millions of cells per voxel if one considers the usual 10^6 cells per mm^3 density commonly referred to in the literature [20]. Managing each individual cell, particularly within the context of treatment, becomes ever more complicated when one considers that such treatments can last several weeks. The associated computational times of the model at mesoscopic scale allow fast tests at the cellular level to be carried out, such as tracking the number of cells in phases G_2 and M of cellular division to optimize the radiotherapy treatment planning. We have shown in this work that based on two FDG PET images (baseline and at 8 days into radiotherapy treatment) the proposed model was capable to approximate the overall heterogeneous oxygen partial pressure within the tumor. Therefore although the proposed model is able to accurately predict the tumor cell evolution during treatment (see Figure 5), their spatial distribution varies between the acquired and simulated images. This deviation may be due to the lack of modelling of specific mechanical processes in the tumor growth both within the tumor but

also in its environment (neighbouring tissue and organs). Such a modelling is necessary to be able to appropriately constrain or increase the spatial distribution of tumor cells during treatment.

In this study, oxygen was considered as an important factor in tumor growth as well as in tumor response during radiotherapy. Although, tumor oxygen distribution is not the only parameter influencing radiotherapy outcome, it is considered as one of the most critical. Oxygen has a major role in cell division, notable as a regulator of hypoxia-inducible factor 1 (HIF-1) and of vascular endothelial growth factor (VEGF) [28]. It has been also clearly established that well-oxygenated solid tumors respond more favorably to radiotherapy than hypoxic ones [29]. On the other hand, it could be appropriate to consider the dynamic changes of the intra-tumor oxygen distribution since it may change during treatment for numerous reasons, such as for example neoangiogenesis. Within this context, hypoxic tumor areas have been reported to include chronic and acute hypoxia [30], [31], with the potential of acute hypoxia changes every few hours or days. However, simulation and imaging studies studying the reproducibility of tumor hypoxia measurements have not demonstrated any effects of acute hypoxia within a few days interval [32], [33].

In the current study, temporal heterogeneity of the oxygen partial pressure was not taken into consideration, since the available image dataset used in this work was acquired over a relatively short period of time (0-15 days into treatment). On the other hand, the proposed model framework is sufficiently flexible to allow the integration of other aspects in the future, one of them being the temporal variation of the pO_2 intra-tumor distribution. The three model scales and their interactions are indeed a sufficiently versatile structure to allow temporal variation of specific biological parameters and their impact. This representation is also particularly relevant for tumor growth modeling based on medical imaging. In other words, a realistic approach would be, if available, to incorporate as an input to the model, information derived from images monitoring different physiological processes. As an example, one can consider the use of [64Cu]Cu-ATSM or [18F]F-MISO PET images in order to obtain data specific to tumor hypoxia [34], [35]. Furthermore, if such image acquisitions are available throughout the radiotherapy treatment they could be also used to account for the dynamic changes in such physiological processes and their influence in the proposed tumor growth model.

Inflammation is another potential phenomenon that may alter tumor oxygen distribution during radiotherapy [36]–[38]. Although inflammation induced by radiotherapy may also have a potential impact on the signal observed in the FDG images, this point was not taken into account in this study because of the lack of specific data regarding rectal cancer. In addition, available data in other cancer models suggests otherwise. Despite been widely considered that reliable FDG PET images cannot be obtained before a few months after radiation therapy due to inflammatory changes, it has been previously demonstrated in lung cancer patients that PET obtained during radiotherapy (7-14 days into treatment) can

identify areas of residual metabolically active tumor [39], [40]. Additionally, it has been shown that this response detected on early FDG PET correlates with final PET response 3 months after completion of treatment.

Tumor spatial localisation, motion and overall shape have not been considered in the presented model, since the precise overall PET image simulation was not a primary objective of this work. In the present work the model evaluation was based on the prediction of the total number of tumor cells. Future work will consider cellular changes in relation to image voxels in order to accurately handle overall tumor size and shape evolutions during treatment.

V. CONCLUSION

An efficient and accurate multi-scale model was proposed for tumor representation and simulation of its temporal global evolution during radiotherapy treatment. Such a model can also be coupled with the prediction of certain tumor global biological parameters such as cellular hypoxia. Temporal heterogeneity of the tumor oxygen partial pressure will be considered in future developments to improve the overall tumor model. Future modifications will also consider variable radio-biology for different tumor cell populations involved in the process; namely quiescent, hypoxic, proliferating and normal cells that can be managed differently. Finally, coupling the proposed voxel-based approach with a model incorporating tumor shape and spatial deformation considering the neighbouring tissue and associated organs would allow the simulation and prediction of complete PET images.

APPENDIX

INITIAL DISTRIBUTION OF CELLS IN EACH PHASE OF CELLULAR CYCLE

Let us note $\alpha_1 = p_1(pO_2)$ and $\alpha_2 = p_2(pO_2)$, the proportions of cells which move from G_1^{15} to S and from G_2^{26} to M. We make the following assumptions:

$$N_{G_1/S}^{15} = \alpha_1 \cdot N_{G_1}^{15}, \quad N_{G_2/M}^{26} = \alpha_2 \cdot N_M^{27}$$

and

$$N_{G_0/G_1} = \gamma \cdot N_{G_0}^{28} \quad 0 \leq \gamma \leq 1$$

Let $\lambda(t) = (\lambda_{G_1}^0(t), \lambda_{G_1}^1(t), \dots, \lambda_M^{27}(t), \lambda_{G_0}^{28}(t)) \in \mathbb{R}^{29}$ the cells distribution in the various phases of cellular division at time t . Keeping the notations of the model we have:

$$\lambda_{G_1}^0(t) = \frac{N_{G_1}^0(t)}{N_{cell}(t)}, \quad \lambda_{G_1}^1(t) = \frac{N_{G_1}^1(t)}{N_{cell}(t)}$$

$$\lambda_M^{27}(t) = \frac{N_M(t)}{N_{cell}(t)}, \dots, \lambda_{G_0}^{28}(t) = \frac{N_{G_0}(t)}{N_{cell}(t)}$$

where, $N_X(t)$ ($X \in \{G_1, S, G_2, M, G_0\}$) depending of $\lambda(t)$. According to the model we have:

$$N_{cell}(t+1) = N_{cell}(t) \cdot \left[1 + \lambda_M^{27}(t) - \lambda_{G_0}^{28}(t) \right]$$

By using the previous expression of $N_{cell}(t + 1)$ and the model, assuming constant distribution, *i.e.* stability condition $\lambda(t + 1) = \lambda(t) = \lambda$ (in this model $\gamma = 1$), we have:

$$\begin{aligned} \lambda_{G_1}^0 &= \frac{2 \cdot \lambda_M^{27}}{1 + \lambda_M^{27}}, & \lambda_{G_1}^1 &= \frac{\lambda_{G_1}^0}{1 + \lambda_M^{27}}, \dots, & \lambda_{G_1}^{15} &= \frac{\lambda_{G_1}^{14}}{\alpha_1 + \lambda_M^{27}} \\ \lambda_S^{16} &= \frac{\alpha_1 \cdot \lambda_{G_1}^{15}}{1 + \lambda_M^{27}}, & \lambda_S^{17} &= \frac{\lambda_S^{16}}{1 + \lambda_M^{27}}, \dots, & \lambda_{G_2}^{26} &= \frac{\lambda_{G_2}^{25}}{\alpha_2 + \lambda_M^{27}} \\ \lambda_M^{27} &= \frac{\alpha_2 \cdot \lambda_{G_2}^{26}}{1 + \lambda_M^{27}}, & \lambda_{G_0}^{28} &= 0 \end{aligned}$$

By expressing all the proportions according to λ_M^{27} and by using:

$$\lambda_{G_1}^0 + \lambda_{G_1}^1 + \dots + \lambda_{G_1}^{14} + \lambda_{G_1}^{15} + \lambda_S^{16} + \dots + \lambda_{G_2}^{25} + \lambda_{G_2}^{26} + \lambda_M^{27} + \lambda_{G_0}^{28} = 1$$

we find that λ_M^{27} satisfies: $f(\lambda_M^{27}) = 0$, and thus deduce remaining proportions.

$$\begin{aligned} f(\lambda_M^{27}) &= 2\lambda_M^{27} \left(\frac{1}{1 + \lambda_M^{27}} + \frac{1}{(1 + \lambda_M^{27})^2} + \dots + \frac{1}{(1 + \lambda_M^{27})^{15}} \right) \\ &+ \dots + 2\lambda_M^{27} \left(\frac{\alpha_1}{(\alpha_1 + \lambda_M^{27})(1 + \lambda_M^{27})^{16}} \right. \\ &\quad \left. + \frac{\alpha_1}{(\alpha_1 + \lambda_M^{27})(1 + \lambda_M^{27})^{25}} \right) \\ &+ 2\lambda_M^{27} \left(\frac{\alpha_1}{(\alpha_1 + \lambda_M^{27})(\alpha_2 + \lambda_M^{27})(1 + \lambda_M^{27})^{25}} \right) \\ &+ 2\lambda_M^{27} \left(\frac{\alpha_1 \alpha_2}{(\alpha_1 + \lambda_M^{27})(\alpha_2 + \lambda_M^{27})(1 + \lambda_M^{27})^{25}} \right) - 1 \end{aligned}$$

ACKNOWLEDGMENT

The authors would like to thank Fabrice Harrouet for his work on the segmentation of the tumor functional volumes used in this work.

REFERENCES

[1] N. Vatandoost *et al.*, “Early detection of colorectal cancer: From conventional methods to novel biomarkers,” *J. Cancer Res. Clin. Oncol.*, vol. 142, no. 2, pp. 341–351, 2016.
 [2] B. Ribba, O. Saut, T. Colin, D. Bresch, E. Grenier, and J. P. Boissel, “A multiscale mathematical model of avascular tumor growth to investigate the therapeutic benefit of anti-invasive agents,” *J. Theor. Biol.*, vol. 243, no. 4, pp. 532–541, 2006.
 [3] C. F. Lo, “Stochastic Gompertz model of tumour cell growth,” *J. Theor. Biol.*, vol. 248, pp. 317–321, 2007.
 [4] A. Gerisch and M. Chaplain, “Mathematical modelling of cancer cell invasion of tissue: Local and non-local models and the effect of adhesion,” *J. Theor. Biol.*, vol. 250, no. 4, pp. 684–704, 2008.
 [5] B. Titz and R. Jeraj, “An imaging-based tumour growth and treatment response model: Investigating the effect of tumour oxygenation on radiation therapy response,” *Phys. Med. Biol.*, vol. 53, no. 17, p. 4471, 2008. [Online]. Available: <http://stacks.iop.org/0031-9155/53/i=17/a=001>
 [6] B. Titz, K. R. Kozak, and R. Jeraj, “Computational modelling of anti-angiogenic therapies based on multiparametric molecular imaging data,” *Phys. Med. Biol.*, vol. 57, no. 19, p. 6079, 2012.
 [7] T. S. Deisboeck, Z. Wang, P. Macklin, and V. Cristini, “Multiscale cancer modeling,” *Annu. Rev. Biomed. Eng.*, vol. 13, pp. 127–155, Aug. 2011.

[8] W.-Y. Tan, W. Ke, and G. Webb, “A stochastic and state space model for tumour growth and applications,” *Comput. Math. Methods Med.*, vol. 10, no. 2, pp. 117–138, 2009.
 [9] H. Lisei and D. Julitz, “A stochastic model for the growth of cancer tumors,” *Stud. Univ. ‘Babes-Bolyai’ Math.*, vol. 53, no. 4, pp. 39–56, 2008.
 [10] E. Konukoglu, M. Sermesant, O. Clatz, J.-M. Peyrat, H. Delingette, and N. Ayache, “A recursive anisotropic fast marching approach to reaction diffusion equation: Application to tumor growth modeling,” in *Information Processing in Medical Imaging*. Springer, 2007, pp. 687–699.
 [11] H. E. Ryan *et al.*, “Hypoxia-inducible factor-1 α is a positive factor in solid tumor growth,” *Cancer Res.*, vol. 60, no. 15, pp. 4010–4015, 2000.
 [12] A. L. Harris, “Hypoxia—A key regulatory factor in tumour growth,” *Nature Rev. Cancer*, vol. 2, no. 1, pp. 38–47, 2002.
 [13] D. L. Bailey, D. W. Townsend, P. E. Valk, and M. N. Maisey, *Positron Emission Tomography*. Springer, 2005.
 [14] J. J. Wille, M. R. Pittelkow, G. D. Shipley, and R. E. Scott, “Integrated control of growth and differentiation of normal human prokeratinocytes cultured in serum-free medium: Clonal analyses, growth kinetics, and cell cycle studies,” *J. Cellular Physiol.*, vol. 121, no. 1, pp. 31–44, 1984. [Online]. Available: <http://dx.doi.org/10.1002/jcp.1041210106>
 [15] L. B. Gardner, Q. Li, M. S. Park, W. M. Flanagan, G. L. Semenza, and C. V. Dang, “Hypoxia inhibits G1/S transition through regulation of p27 expression,” *J. Biol. Chem.*, vol. 276, no. 11, pp. 7919–7926, 2001.
 [16] S. Benzekry *et al.*, “Classical mathematical models for description and prediction of experimental tumor growth,” *PLoS Comput. Biol.*, vol. 10, no. 8, p. e1003800, 2014.
 [17] J. P. Kirkpatrick, J. J. Meyer, and L. B. Marks, “The linear-quadratic model is inappropriate to model high dose per fraction effects in radiosurgery,” in *Seminars Radiat. Oncol.*, vol. 18, no. 4, pp. 240–243, 2008.
 [18] M. Guerrero and X. A. Li, “Extending the linear–quadratic model for large fraction doses pertinent to stereotactic radiotherapy,” *Phys. Med. Biol.*, vol. 49, no. 20, p. 4825, 2004.
 [19] H. Mi, C. Petitjean, B. Dubray, P. Vera, and S. Ruan, “Prediction of lung tumor evolution during radiotherapy in individual patients with PET,” *IEEE Trans. Med. Imag.*, vol. 33, no. 4, pp. 995–1003, Apr. 2014.
 [20] I. Espinoza, P. Peschke, and C. Karger, “A voxel-based multiscale model to simulate the radiation response of hypoxic tumors,” *Med. Phys.*, vol. 42, no. 1, pp. 90–102, 2015.
 [21] M. C. Joiner and A. van der Kogel, *Basic Clinical Radiobiology*. London, U.K.: Hodder, 2009.
 [22] I. Finlay, D. Meek, F. Bruntont, and C. McArdle, “Growth rate of hepatic metastases in colorectal carcinoma,” *Brit. J. Surg.*, vol. 75, no. 7, pp. 641–644, 1988.
 [23] E. Diederich *et al.*, “Dynamics of microvascular oxygen partial pressure in contracting skeletal muscle of rats with chronic heart failure,” *Cardiovascular Res.*, vol. 56, no. 3, pp. 479–486, 2002.
 [24] M. Hatt *et al.*, “Accurate automatic delineation of heterogeneous functional volumes in positron emission tomography for oncology applications,” *Int. J. Radiat. Oncol. Biol. Phys.*, vol. 77, no. 1, pp. 301–308, 2010.
 [25] M. Hatt, C. C. le Rest, A. Turzo, C. Roux, and D. Visvikis, “A fuzzy locally adaptive Bayesian segmentation approach for volume determination in PET,” *IEEE Trans. Med. Imag.*, vol. 28, no. 6, pp. 881–893, Jun. 2009.
 [26] J. Nossent, P. Elsen, and W. Bauwens, “Sobol’ sensitivity analysis of a complex environmental model,” *Environ. Model. Softw.*, vol. 26, no. 12, pp. 1515–1525, 2011.
 [27] I. M. Sobol, “Global sensitivity indices for nonlinear mathematical models and their Monte Carlo estimates,” *Math. Comput. Simul.*, vol. 55, nos. 1–3, pp. 271–280, 2001.
 [28] A. Laurent *et al.*, “Controlling tumor growth by modulating endogenous production of reactive oxygen species,” *Cancer Res.*, vol. 65, no. 3, pp. 948–956, 2005.
 [29] W.-J. Koh *et al.*, “Evaluation of oxygenation status during fractionated radiotherapy in human nonsmall cell lung cancers using [F-18]fluoromisonidazole positron emission tomography,” *Int. J. Radiat. Oncol. Biol. Phys.*, vol. 33, no. 2, pp. 391–398, 1995.
 [30] F. Pajonk, E. Vlashi, and W. H. McBride, “Radiation resistance of cancer stem cells: The 4 R’s of radiobiology revisited,” *Stem Cells*, vol. 28, no. 4, pp. 639–648, 2010.
 [31] C. Bayer, K. Shi, S. T. Astner, C.-A. Maftei, and P. Vaupel, “Acute versus chronic hypoxia: Why a simplified classification is simply not enough,” *Int. J. Radiat. Oncol. Biol. Phys.*, vol. 80, no. 4, pp. 965–968, 2011.

- [32] D. Mönnich, E. G. Troost, J. H. A. M. Kaanders, W. J. G. Oyen, M. Alber, and D. Thorwarth, "Modelling and simulation of the influence of acute and chronic hypoxia on [^{18}F]fluoromisonidazole PET imaging," *Phys. Med. Biol.*, vol. 57, no. 6, p. 1675, 2012.
- [33] S. Okamoto *et al.*, "High reproducibility of tumor hypoxia evaluated by 18f-fluoromisonidazole pet for head and neck cancer," *J. Nucl. Med.*, vol. 54, no. 2, pp. 201–207, 2013.
- [34] K. S. C. Chao *et al.*, "A novel approach to overcome hypoxic tumor resistance: Cu-ATSM-guided intensity-modulated radiation therapy," *Int. J. Radiat. Oncol. Biol. Phys.*, vol. 49, no. 4, pp. 1171–1182, 2001.
- [35] A. Paesen and G. De Loof, "A new hypoxia imaging agent with high membrane permeability and low redox potential," *Int. J. Invertebrate Reprod. Develop.*, vol. 14, pp. 267–277, 1988.
- [36] F. Rödel, L. Keilholz, M. Herrmann, R. Sauer, and G. Hildebrandt, "Radiobiological mechanisms in inflammatory diseases of low-dose radiation therapy," *Int. J. Radiat. Biol.*, vol. 83, no. 6, pp. 357–366, 2007.
- [37] C.-H. Heldin, K. Rubin, K. Pietras, and A. Östman, "High interstitial fluid pressure—An obstacle in cancer therapy," *Nature Reviews. Cancer*, vol. 4, no. 10, p. 806, 2004.
- [38] J. Overgaard and M. R. Horsman, "Modification of hypoxia-induced radioresistance in tumors by the use of oxygen and sensitizers," *Seminars Radiat. Oncol.*, vol. 6, no. 1, pp. 10–21, 1996.
- [39] A. van Baardwijk *et al.*, "Time trends in the maximal uptake of FDG on PET scan during thoracic radiotherapy. A prospective study in locally advanced non-small cell lung cancer (NSCLC) patients," *Radiotherapy Oncol.*, vol. 82, no. 2, pp. 145–152, 2007.
- [40] F.-M. S. Kong *et al.*, "A pilot study of [^{18}F]fluorodeoxyglucose positron emission tomography scans during and after radiation-based therapy in patients with non-small-cell lung cancer," *J. Clin. Oncol.*, vol. 25, no. 21, pp. 3116–3123, 2007.